THEORETICAL LIMITS AND DESIGN METHOD FOR LEVITATION OF A SLIT BASED METALENS

MSc Thesis

by

Nina SIMON

to obtain the degree of Master of Science
at the Delft University of Technology,
to be defended on December 9th, 2025 at 9:30 AM

Student Number:	5144744	
Thesis advisors:	Dr. R.A. Norte,	TU Delft, 3mE faculty
	Ir. L. Norder	TU Delft, 3mE faculty
Thesis committee:	Dr. A. Adam	TU Delft, Physics faculty
	Dr. F. Maucher	TU Delft, 3mE faculty

ACKNOWLEDGEMENTS

I would like to express my sincere gratitude to all who helped and supported me during my thesis project. It has been a long and truly educational journey, which would not have been possible without the people around me.

First and foremost, I want to thank my supervisors, Richard Norte and Lucas Norder, for guiding me throughout these seven months. To Richard for offering the opportunity to work on this subject and for your enthusiasm for this strange idea to pull things with lasers. And to Lucas, for our weekly meetings which were critical in guiding me forward on the project. A special thanks also goes out to the people in the Norte lab, for the weekly meetings which offered fun insights into varied projects and good help when needed.

I want to thank my EWI study group for essentially being my support group through all the times that I incapacitated my laptop by spilling water on it. So, thanks to Sjoerd, Nick, Jueun, Remco, Laura, Koen, Gab, Thomas, Santo, Valery, Wendy, Joos, and others for the good vibes, moral support, and for the many necessary distractions. I want to thank Pepijn for listening to my thesis stories, my siblings and finally my parents, Loes, for her unwavering support and Paul for being a driving force and motivation source throughout my entire studies.

Nina Simon
November, 2025

SUMMARY

Optical manipulation has recently become indispensable in various disciplines and optical levitation specifically offers many possibilities in highly sensitive motion detection. The counterintuitive "tractor beams" have therefore captivated research due to their possible new approach to levitation. The key principle in designing an optical pulling force is the enhancement of the forward momentum by the pulled object. The idea of using the light modulating capacities of a metalens to increase the forward momentum has been proposed in literature. Here, a simple theoretical analysis is done to give a simple formula for the optical pulling force (OPF) generated by a one-dimensional metalens. From there two parameters are determined to be limiting for the OPF generated by a metalens: the transmissivity and the numerical aperture of the lens. A large numerical aperture and a large transmissivity of the lens appear to be critical in obtaining an apparent optical pulling force. Unlike in traditional optical trapping, where the object must be confined at the focal spot and is therefore limited in size by diffraction and high local intensities, the metalens considered here is not placed at the focus itself. This configuration relaxes the geometric and diffraction-related constraints of conventional trapping and shifts the difficulty from maintaining a tightly confined focus to engineering a lens that can efficiently redirect momentum over a large angular range. A workflow to design one-dimensional slit-based metalenses is proposed taking into consideration the results from the theoretical analysis. The optimized metalens design achieves an accurate focal point, exhibiting a deviation of only 2.88% from the targeted focal length. Which is a competitive error compared to literature. The analytical formula predicts that optimized lenses can generate a linear force on the order of 10^{-12} Nm/W, in good agreement with values reported in literature, thereby supporting the validity of the analytical model.

CONTENTS

1

INTRODUCTION

Levitating objects in vacuum creates an environment in which their motion can be measured with very high precision. Ongoing developments in optical levitation are pushing this sensitivity even further, enabling the detection of minute perturbations [1], [2]. When operated in vacuum, levitated systems exhibit high mechanical quality factors, making them sensitive to very small perturbations and therefore promising for precision measurement and sensing applications[3], [4]. Using light to support and manipulate objects without physical contact enables precise and remote control of motion [5], [6]. However, these demonstrations have so far been largely limited to nanoparticles and microspheres [2]. To advance fields such as light-sail propulsion [7] and optomechanics, there is a need for techniques that provide the same precision measurements and motion control currently achievable for nanoparticles, but applied to larger, engineered optical structures. In emulated low-gravity environments, complex questions such as stable flight dynamics and self-stabilization can be complicated by the external forces introduced by mechanical or magnetic supports. A promising way to overcome this is to place the object in an optically levitated state using radiation pressure.

Many fields use forwards optical radiation pressure as an indispensable tool; aerospace engineering [8], optomechanics [9], biology[10] and quantum physics [11]. Recently, the counter-intuitive concept of pulling objects toward the light source, against the direction of the light's momentum, was introduced with the Optical Pulling Force (OPF) [12], also known as 'tractor beams'. These have been getting more attention due to their potential applications in advanced optical manipulation techniques[13] like remote mass transportation[14] or optical sorting[15] and can therefore be considered as a valid candidate for levitation.
In literature, three main ways have been proposed to achieve a tractor beam: using structured light beams [16], designing the interaction environment [17], or engineering the optical characteristics of the object itself [18]. In this work we focus on the last strategy. This method involves engineering the optical characteristics of the moved object itself to maximize the forward momentum of the scattered light. In according to the linear momentum conservation a backward pulling force can be generated when the forward momentum is maximized. This increased forward momentum is achievable using complex methods like gain media [18], [19] or core-shell microspheres [20]. Alternatively, a simpler approach like a lens could increase the forward momentum by focusing the light appropriately [21], [22]. However, traditional lenses rely on bulk material thickness, inherently making them large and impractical for lifting and moving applications.

Recently, significant progress in nanophotonics has enabled alternatives such as metalenses [23] and photonic crystals. These offer a thinner and more versatile option than traditional optics as they operate on the nanoscale to structure light. These devices are composed of small repeating building blocks called unit-cells. These unit-cells define the local optical response by varying the refractive index. Literature has shown that complex metasurface geometries can be engineered to focus light with high efficiency [24], [25]. optical manipulation generally needs high powered lasers, silicon nitride is a promising material for this application because of its low absorption[26]. It also has been proven a suitable platform for high-contrast subwavelength patterning [9], [27]. The work by Peng et al. [28] demonstrates, through simulation, that a metalens composed of silicon nanopillars can experience a net optical pulling force directed toward the light source. However, these metalenses rely on intricate two-dimensional nanostructures that complicate both the design process and fabrication. Furthermore, the sizes are limited to the microscale. This project aims to give

an scalable design workflow of metalenses capable of being pulled toward the light source but using a simpler one-dimensional (1D) grating approach pattern in silicon nitride.

In developing a metalens capable of exhibiting an optical pulling force, several limitations are bound to play a role. One of which is the inherent trade-off between transmittance, which is crucial for generating a strong optical pulling force, and the refractive index, which is essential for achieving full phase control. This report begins by deriving a simplified theoretical model that establishes the fundamental limits of generating a negative (pulling) optical force on a metalens. This analytical treatment yields a closed-form expression for the pulling force, an expression which, to the best of our knowledge, has not previously been formulated for metalenses. It then outlines a computational workflow for designing one-dimensional metalenses that satisfy these constraints. Finally, the feasibility of experimentally levitating such a metalens is assessed.

2

ENGINEERING AN OPTICAL PULLING FORCE

This chapter introduces the fundamental concept of the optical pulling force, a counter-intuitive phenomenon where light exerts a force that pulls an object towards the source. Achieving this effect requires engineering the light's momentum upon interaction with a scatterer, which we explore through the design of a metalens as a light-redirecting device.

2.1. THE MECHANISMS OF GENERATING OF AN OPTICAL PULLING FORCE

Consider a scenario in which a plane wave propagates along the z-direction and interacts with an black box scatterer as illustrated in Figure 2.1a. A negative (pulling) force can be achieved if the momentum of the outgoing light along the z-direction exceeds that of the incoming beam. This situation is created by illuminating the object at an angle and engineering the scatterer such that all the light is collimated straight ($\overrightarrow{k_{scat}}$ is parallel to the z axis). If the scatterer is a non-absorbing structure capable of redirecting light in this way with no reflection, by conservation of momentum, a negative force will be generated [22], as described by the following relation:

$$k_{inc}\cos\theta = k_{sca} + k_{lens} \tag{2.1}$$

where θ is the incident angle, k_{inc} is the momentum of the incoming light, k_{sca} the momentum of the outgoing light. The force exerted on the scatterer becomes

$$F_z = \frac{P}{c}(\cos\theta - 1) \tag{2.2}$$

Where P is the power of the incoming light, c is the speed of light.

Therefore, in order to obtain the desired OPF there are two main objectives: the object must scatter the incident light such that the resulting phase function leads to enhanced forward momentum. Secondly, in order to collimate the incoming light in the forward direction, the device must be highly transmissive, meaning that the light and its momentum are transmitted and not reflected by the device. Hence the idea for a converging lens which collimates an incoming diverging beam parallel to the z-direction (Figure 2.1b). We propose a thin metalens as a way to generate this OPF. In an effort to make the simplest shape to fabricate in the lab as possible, the choice is made to make the design one dimensional, effectively making the dielectric value vary only in one direction by etching slits into optical material along the x-axis (Figure 2.1c). Silicon is the usually preferred material for dielectric metasurfaces due to its high refractive index and low absorption loss. It has been demonstrated that a one-dimensional high-contrast photonic grating on Si membrane can be made focusing by chirping the periodic structure [25][24][29]. In the visible range, lower index dielectrics, such as silicon nitride [30] or titanium dioxide[31] are often used since they are transparent in these regions. Silicon nitride has a refractive index of $n \approx 2$[9], which is lower than that of silicon, which will limit the phase wavefront manipulation capability [27], but its really low optical absorption makes it more suited to a transmissive lens [32]. The wavelength used to do the simulations is 1.070 μm as this is commonly used for high power applications.

2

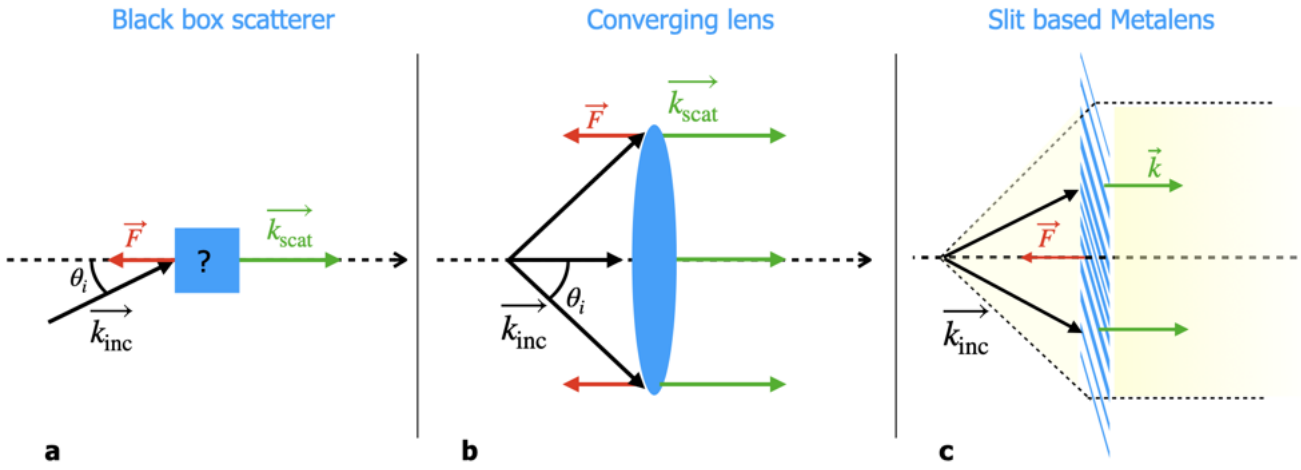

Figure 2.1: Conceptual Illustration of Optical Pulling Force (OPF) and Metalens Action. **(a)** A conceptual "black box" optical device that converts incident waves into waves propagating along the positive z-axis. When the net scattering results in an overall increase in forward momentum, the resulting optical force exerted on the device is negative (a pulling force). **(b)** A traditional converging lens demonstrates this effect by enhancing the forward scattering (focusing) of the waves from an incoming diverging beam. **(c)** A thin metalens achieves the same optical function as a traditional converging lens (focusing the incoming beam) but without the volume and weight associated with the bulkiness of a traditional glass optic.

2.2. CREATING A CONVERGING METALENS

In order to effectively redirect the light as a converging lens would, the light transmitted through the device must constructively interfere at a focal point. Therefore, the phase distribution of the metalens should be equal to that of a conventional spherical lens [33]:

$$\phi(x) = \frac{2\pi}{\lambda}\left(\sqrt{x^2+f^2} - f\right) \tag{2.3}$$

where λ is the wavelength, f is the focal length and x defines the location of a point on the dielectric surface. This target phase is plotted in Figure 2.2b.

To achieve this the dielectric surface is partitioned in sub-wavelength pieces, called unit-cells, which here are slits surrounded by optical material as displayed in Figure 2.2a.

These unit-cells are positioned periodically, with a center-to-center distance p such that the phase at the corresponding position on the x-axis matches the target phase given by equation 2.3 as schematized in Figure 2.2b. The width of the slits per unit-cell allows to control the phase and transmission of light through the sample. Both these properties can be calculated using Rigorous Coupled Wave Analysis (RCWA) [34] as detailed in appendix A.

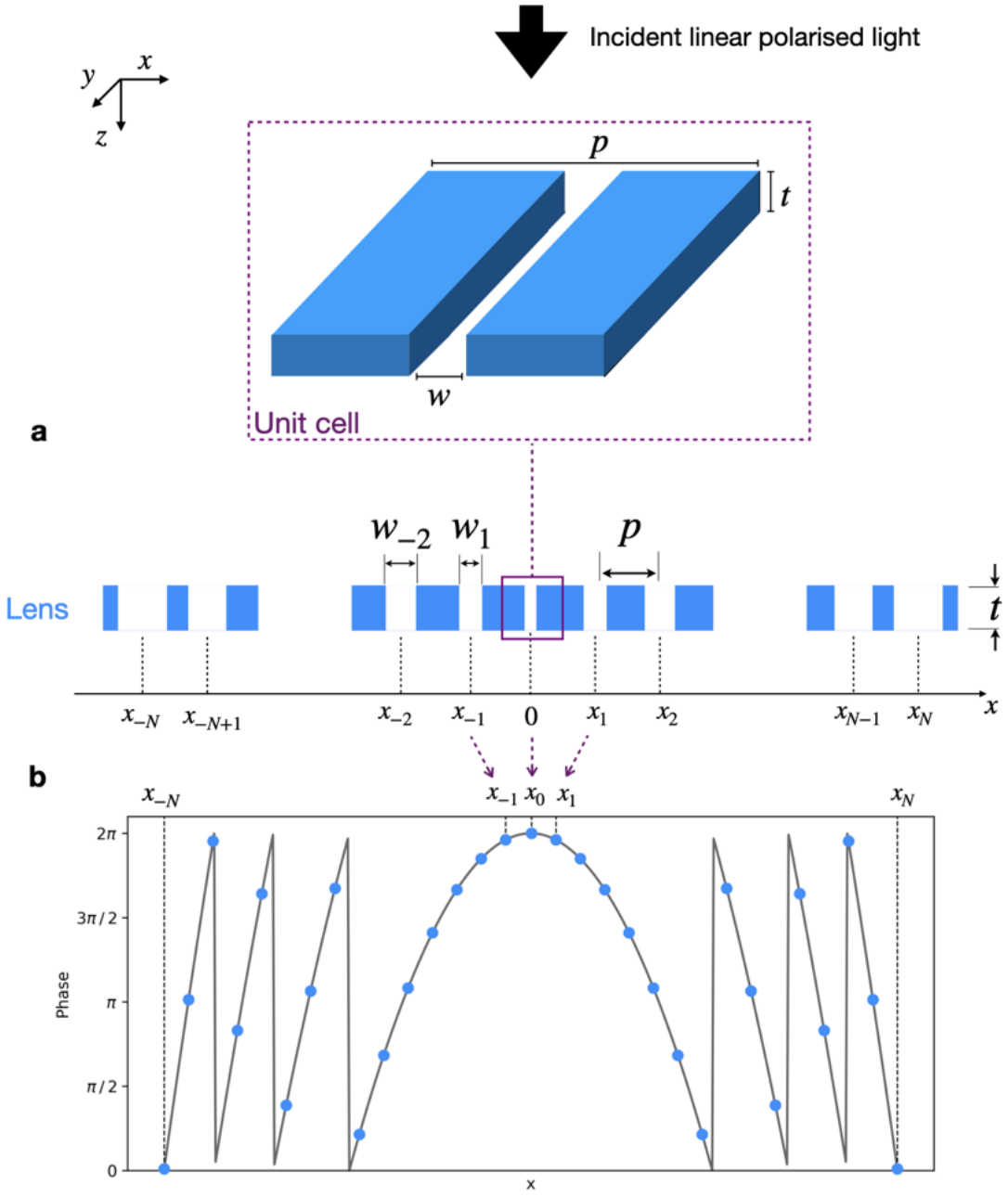

Figure 2.2: Metalens Unit-Cell Design and Phase Implementation. **(a)** Schematic diagram of the fundamental unit-cell employed in the etalens design. Key geometric parameters are highlighted: w denotes the width of the slit, p represents the period (the distance between unit-cell centers and its lateral size), and t indicates the thickness of the unit-cell, which defines the overall thickness of the metalens. **(b)** Visualization of the quasi-periodic arrangement of silicon nitride grating unit-cells (blue) in air. Each unit-cell at position x_i has a slit width w_i and the cells are separated by period p. The black curve illustrates the ideal target phase $\phi_{\text{tar}}(x)$ mod 2π. The circles represent the discrete phases of the individual unit-cells as they are placed along the lens aperture, approximating the continuous target profile.

3

LIMITS OF OPTICAL PULLING GENERATED BY A METALENS

This chapter introduces the momentum conservation principles governing the interaction between light and a metalens to establish the theoretical limits on achieving an OPF. By analyzing the force contribution across a diverging incident beam, we derive a relationship between metalens transmissivity and the required numerical aperture necessary for generating a net attractive force.

To describe the conditions under which a metalens can generate an optical pulling force, one can start from the momentum conservation law for the incident, reflected, and transmitted fields [22][35]. Since the lens can not be 100% transmissive, the reflected orders are taken into account. Consider a light ray at an incident angle θ_i on a grating locally considered as periodic. The conservation of momentum can be expressed as:

$$\vec{k}_{\text{grating}} = \sum_m \vec{k}_{r,m} + \vec{k}_i + \vec{k}_t \tag{3.1}$$

where $\vec{k}_i$ ($\vec{k}_t$) is the incident (transmitted) wave vector , the transmitted wave vector and $\vec{k_{r,m}}$ the reflection into multiple diffraction orders. The wave vectors are schematized in Figure. 3.1a. For every incident angle θ_i the force on the grating becomes[35]:

$$\vec{F}_i = \frac{P_i}{ck}\left(\vec{k}_i - \sum_m \eta_m \vec{k}_{r,m}\right), \quad \text{where } |\vec{k}_i| = |\vec{k}_t| = |\vec{k}_{r,m}| = k = \frac{2\pi}{\lambda} \tag{3.2}$$

with $\eta_m = \frac{P_m}{P_i}$ the efficiency of the reflected orders (such that $\sum_m \eta_m = 1$); P_i (P_m) si the incident beam power and c the speed of light. The lens is assumed to successfully collimate the incoming beams at all angles. The pulling force is lowest when the pushing force is maximal, which happens when the reflection for all orders is normal ($\theta_{r,m} = 0$) (see figure 3.1b). Using this assumption the formula for the force can be simplified to a version in the worst-case scenario, which should lead to an estimate of the lowest pulling force achievable (further detailed derivation given in Appendix B)

$$F_z(\theta_i) = \frac{P_i}{c}\left(\cos\theta_i - 2T + 1\right). \tag{3.3}$$

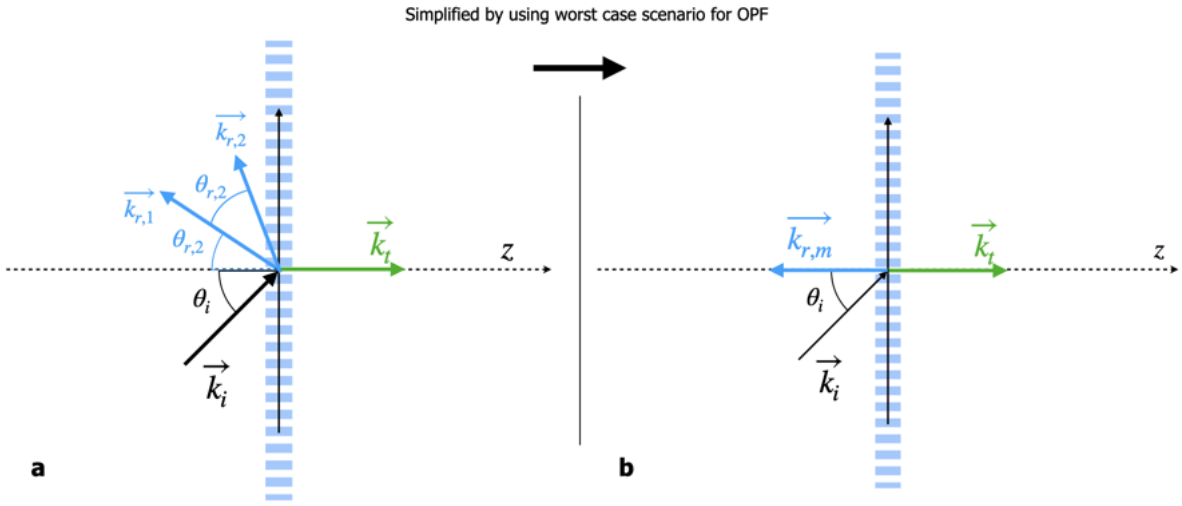

Figure 3.1: Wave-vector geometry at a Grating and Optical Pulling Force (OPF). (a) Illustration of an incident plane wave interacting with a locally periodic grating structure. The key wave vectors are shown: the incident vector $\vec{k}_i$, the transmitted vector $\vec{k}_t$, and the reflected diffraction orders $\vec{k}_{r,m}$. The interaction is governed by the angle of incidence θ_i. **(b)** A simplified wave vector geometry specifically depicting the "worst-case scenario" for the optical pulling force (OPF) phenomenon. In this unfavorable condition, the reflected diffraction orders ($\vec{k}_{r,m}$) are all oriented perpendicular to the lens surface, leading to a maximal negative contribution to the net optical force.

This work aims to use an incident diverging light beam constituted by a sum of plane waves with varying incident angles θ_i, which all contribute differently to the force along z. A plane wave with normal incidence ($\theta_i = 0$) can only create a pushing force while waves with close to parallel incidence ($\theta_i = \pi/2$) contribute the most effectively to the negative force as given by equation 3.3. Obviously, there should exist an angle of incidence $0 < \theta_{\min} < \pi/2$ at which the pushing and pulling force negate and the plane wave contribution to the negative force is zero[22]. Therefore there is only a negative force on the parts of the lens where $\theta_i > \theta_{\min}$. To estimate $\theta_{\min}$ the formula of the force is set to zero:

$$\begin{aligned} F_z(\theta_{\min}) &= 0 \\ \cos\theta_{\min} &= 2T - 1 \end{aligned} \tag{3.4}$$

This gives an estimate for the minimum angle of the negative force $\theta_{\min} = \cos^{-1}(2T-1)$ this is schematized in Figure. 3.2. The total force exerted on the lens is given by the sum over all angles of the diverging beam. The negative force generated on the outside of the lens (where $\theta_i > \theta_{\min}$) needs to counteract the positive force at the inside of the lens (where $\theta_i < \theta_{\min}$). Assuming P_i is constant across the angle interval and defining $\theta_{\max} = \tan^{-1}\left(\frac{D}{2f}\right)$ as the largest angle of the diverging beam as plotted in Figure. 3.2 (such that $\sin\theta_{\max} = \text{NA}$).

$$F_{z,\text{tot}} = \frac{2P}{c}(\sin\theta_{\max} + \theta_{\max}(1-2T)) = \frac{2P}{c}(\text{NA} + \sin^{-1}(\text{NA})(1-2T)) \tag{3.5}$$

This force is plotted in Figure. 3.3 as a function of the transmissivity T and the maximal angle $\theta_{\max}$. Above the blue line the force is a negative pulling force, while beneath, there is a positive pushing force. For low transmissivities of the lens the numerical aperture of the lens needs to be large to compensate for the pushing forces at the center of the lens (see Figure. 3.2), outlining a design requirement. Therefore, it becomes apparent how achieving high transmissivity in the lens design is important. Reaching high transmissivities can prove to be a challenge, especially since there is a trade off between phase manipulation and transmissivity of the lens. Therefore, after having determined the reachable transmissivity for the lens design, this plot

helps determine how large θ_{max} should be and thus the value for the numerical aperture ($\theta_{max} = \sin^{-1}(\text{NA})$). The dimensions for the focal distance and the diameter of the lens are also limited using $\tan\theta_{max} = \left(D/2f\right)$. The lower the transmissivity the lower the stricter the requirements on the dimensions become, meaning the requirement for the numerical aperture gets larger.

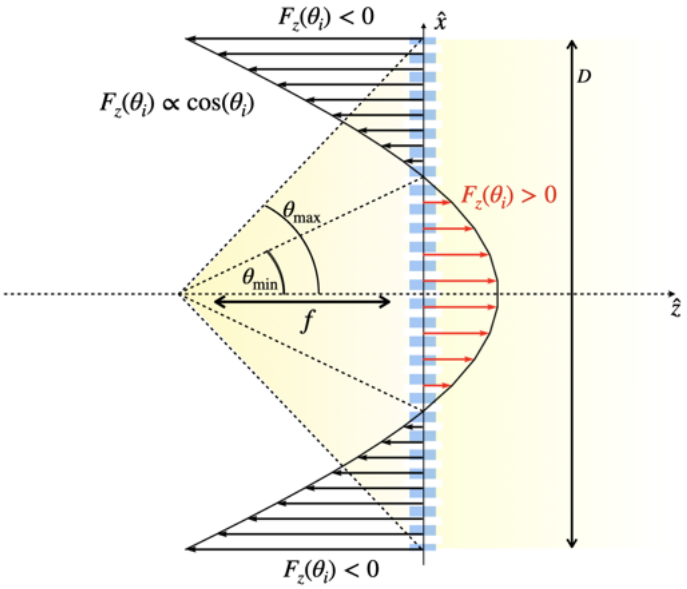

Figure 3.2: Push vs pull contributions vs angle Schematic separation of angular regions contributing to pushing ($0 \leq \theta < \theta_{min}$) and pulling ($\theta_{min} \leq \theta \leq \theta_{max}$) under the worst-case reflection assumption. θ_{min} is dictated by the transmissivity in $\theta_{min} = \cos^{-1}(2T-1)$ and θ_{max} is related to the numerical aperture of the system such that $\tan\theta_{max} = \left(D/2f\right)$ where f is the focal distance of the lens and D the diameter of the lens.

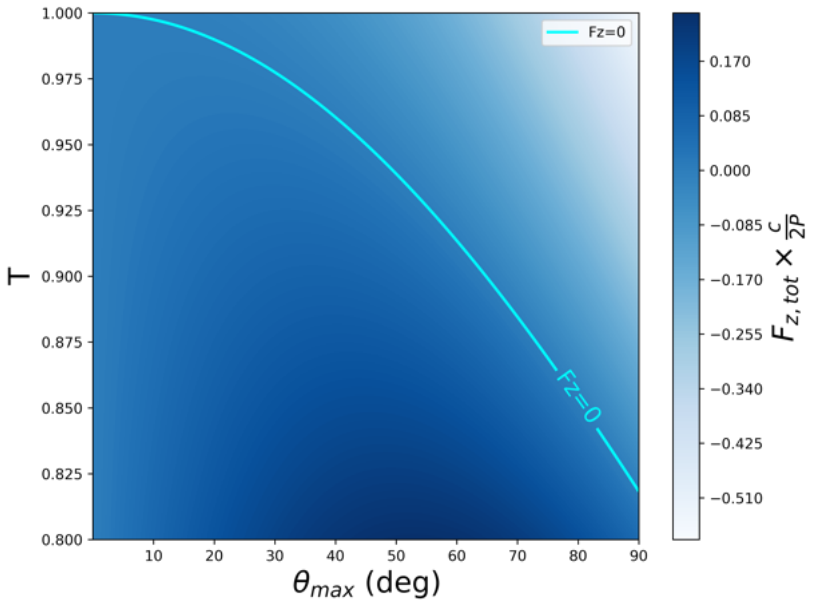

Figure 3.3: Net force over the whole lens versus transmissivity and numerical aperture. As given by equation 3.5 the force over the whole lens is plotted. The light blue line is the points of the parameter space where the force experienced by the metalens is null. T is the transmissivity of the lens, θ_{max} is related to the numerical aperture of the system by $\theta_{max} = \sin^{-1}(\text{NA})$.

In conclusion, the theoretical analysis showed that there were limits to the optical pulling force that could be generated by a metalens. As the strength of the OPF is related to the incoming angle (or numerical aperture, NA) of the diverging beam, the force exerted by the high-angle light at the outer parts of the lens needs to compensate for the predominantly positive (pushing) force generated by the low-angle light at the center of the lens. Therefore, there are two primary factors influencing the achievable OPF magnitude: the larger the NA, the larger the pulling force; and the larger the transmissivity of the metalens, the larger the pulling force.

4

SIMULATING A ONE-DIMENSIONAL LENS

This Chapter details the two-stage process for designing the metalens: first, optimizing the fundamental unit-cell geometry to meet performance criteria, and second, building the complete lens structure and validating its focusing capability through simulation. The goal of maximizing transmissivity and numerical aperture, established in the theoretical analysis, drives the design choices.

4.1. OPTIMIZATION OF PERIOD AND THICKNESS

From the analytical analysis in Chapter 3 the importance of achieving a high transmissivity was highlighted; the lower the transmissivity of the lens is, the stricter the requirements for the numerical aperture of the lens are. This led to an optimization scheme of the parameters of the one-dimensional design, which have an impact on the transmissivity, the period, and the thickness of the lens. Sweeps were done over a parameter space in order to determine the optimal (p, t) combination (see Appendix C for detailed optimization scheme). The pair was optimized using two criteria: satisfy a minimum phase span of $\Delta\phi > 0.8\pi$ which corresponds to one of the smaller phase intervals reported in literature for a silicon nitride focusing grating [9], showing that this phase reach was sufficient for focusing. Secondly, maximizing T to keep the condition on the numerical aperture defined in figure 3.3 minimized. The results of these sweeps and the optimization process are summarized in figure 4.1; on the left, the transmissivity superposed with the phase contour lines (in black) is plotted, on the right the Pareto plots used to illustrate the optimal choice made is shown. The red dot represents the chosen combination of parameters; $(p, t) = (0.456\ \mu\text{m}, 0.583\ \mu\text{m})$. For these parameters $T_{\text{min}} = 0.915$, and the maximum angle is $\theta_{\text{max}} = 1.039$ rad $\approx 59°$. From the sweep results there seems to be a periodicity with a gradual decline of transmissivity as the thickness grows but the phase interval gets larger as the thickness grows, here a clear trade-off is identified between phase manipulation and transmissivity.

4.2. BUILDING THE UNIT-CELL LIBRARY AND SIMULATING THE WHOLE LENS

A unit-cell library documents the unit-cell parameters, in this case, the width of the slit, with the associated phase transformation and transmissivity. This documentation allows the placements along the target phase profile as described in Figure 2.2.

Using the optimal period and thickness determined in the preceding steps, a unit–cell library is constructed by sweeping the duty cycle $dc = w/p$ (ratio of slit width to period) and recording $\{dc, T(dc), \phi(dc)\}$. These functions are interpolated and plotted in Figure 4.2a. In this figure, the phase reach of the unit-cell library does not cover the whole 2π interval, here it only covers $\Delta\phi = 3.01\text{rad} \approx 0.96\pi$, this is a result of the trade-off with transmissivity. The phases are sorted and divided into uniform bins spanning $[\phi_{\text{min}}, \phi_{\text{max}}]$ each bin corresponding to a unit-cell of the library, which is represented by the purple dots in the figure. The unit-cells centers are then placed as schematized in figure Figure 2.2b. The resulting phase shape for an instance of focal distance is presented in Figure Figure 4.2b. The truncated phase limits the amount of the target phase profile that can be covered and therefore limits diameter of the lens. The limited diameter of the lens and, therefore the amount of placed unit-cells can have an impact on how accurately the phase transformation of the created lens matched the target phase transformation given by 2.3. Therefore, a plane electric field is simulated to fall on the lens to determine the accuracy of the achieved focal point.

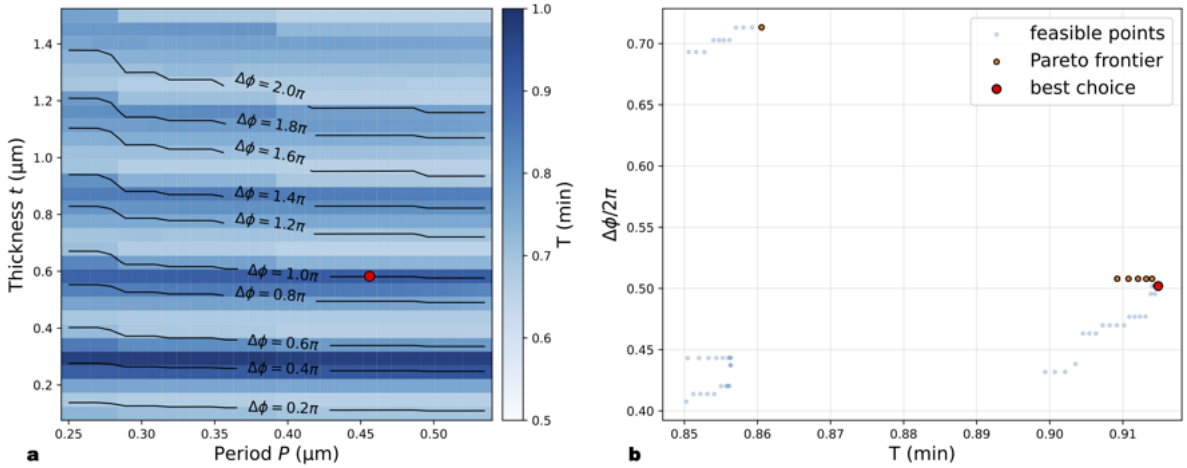

Figure 4.1: Optimization Summary for metalens Period and Thickness. **(a)** This map shows the minimum transmissivity (T_{min}) achieved across various combinations of period (p) and thickness (t). Superposed on this map are black contour lines indicating the associated phase range coverage. The red dot identifies the chosen optimal pair: $(p, t) = (0.456\ \mu\text{m}, 0.583\ \mu\text{m})$, selected for maximizing phase coverage while maintaining high transmission. **(b)** This plot displays the Pareto front (the set of non-dominated solutions) for the feasible design points, summarizing the trade-off between design objectives. The same optimal pair of period and thickness (p, t) selected from the left plot is marked in red, indicating its performance relative to the Pareto optimal boundary.

Generally, the inherent periodicity of RCWA does not allow the simulation of a non-periodic sample. But a few adjustments to the simulated cell allow to bypass the periodicity requirement and simulate whole lenses as a "supercell". To bypass the periodicity of the simulation, padding regions several times larger than the lens area (typically three times the lens diameter) filled with a homogeneous, highly absorbing medium are added around the patterned unit-cell, as shown in Figure 4.3a, to suppress any transmitted light. More details about this approach can be found in Appendix D . In this image, the field amplitude $|E(x,z)|^2$ over the full region behind the one-dimensional metalens is shown, from which the on-axis intensity profile $I(z)$ is extracted and smoothed to suppress noise, allowing the focal distance to be identified as the position of the global maximum of $I(z)$.

To assess the workflow's accuracy, a series of full-lens simulations were conducted on lenses designed for various target focal lengths (f_{target}), and their focal points were measured. These designs were generated by mapping the desired phase distribution onto the lens aperture using the previously established unit-cell library.

The effective focal length (f_{eff}) showed an average deviation of 11.7% from f_{target} (Figure 4.3b). This confirms the method's validity, as the simulated focal length remains close to the target value across the full focal-length range. The observed discrepancy likely stems from the limited lens diameter, which is constrained by the restricted phase coverage achievable with the current unit-cell library.

Furthermore, as established in Chapter 3, generating an optical pulling force requires a minimum numerical aperture (NA) for a given minimum transmissivity. For a minimum transmissivity of $T_{\text{min}} = 0.915$, this minimum is a large NA ≈ 0.86 ($\theta_{\text{max}} = 1.039$ rad $\approx 59°$). This NA cannot be reached with the actual method due to the limiting phase reach interval and the resulting limited diameter.

The simulation of larger metalenses involves approximating the spherical phase target. The algorithm wraps the target phase to the closest available unit-cell phase until a specified radius of 130% of the initial design radius is reached. For each position x along the lens, the algorithm determines the wrapped target phase and selects the unit-cell whose phase bin contains this value. This procedure ensures a unit-cell is placed at each location up to the desired lens radius, resulting in a truncated phase profile as shown in Figure 4.4a. The results of this sweep, shown in Figure 4.4c, indicate that the average deviation decreased significantly, from 11.7 % to only 2.88 %. This confirms that the wrapped-phase approach enables the construction of larger lenses, allowing the designed focal point to more closely match the target value and to satisfy the optical pulling force requirements for the numerical aperture.

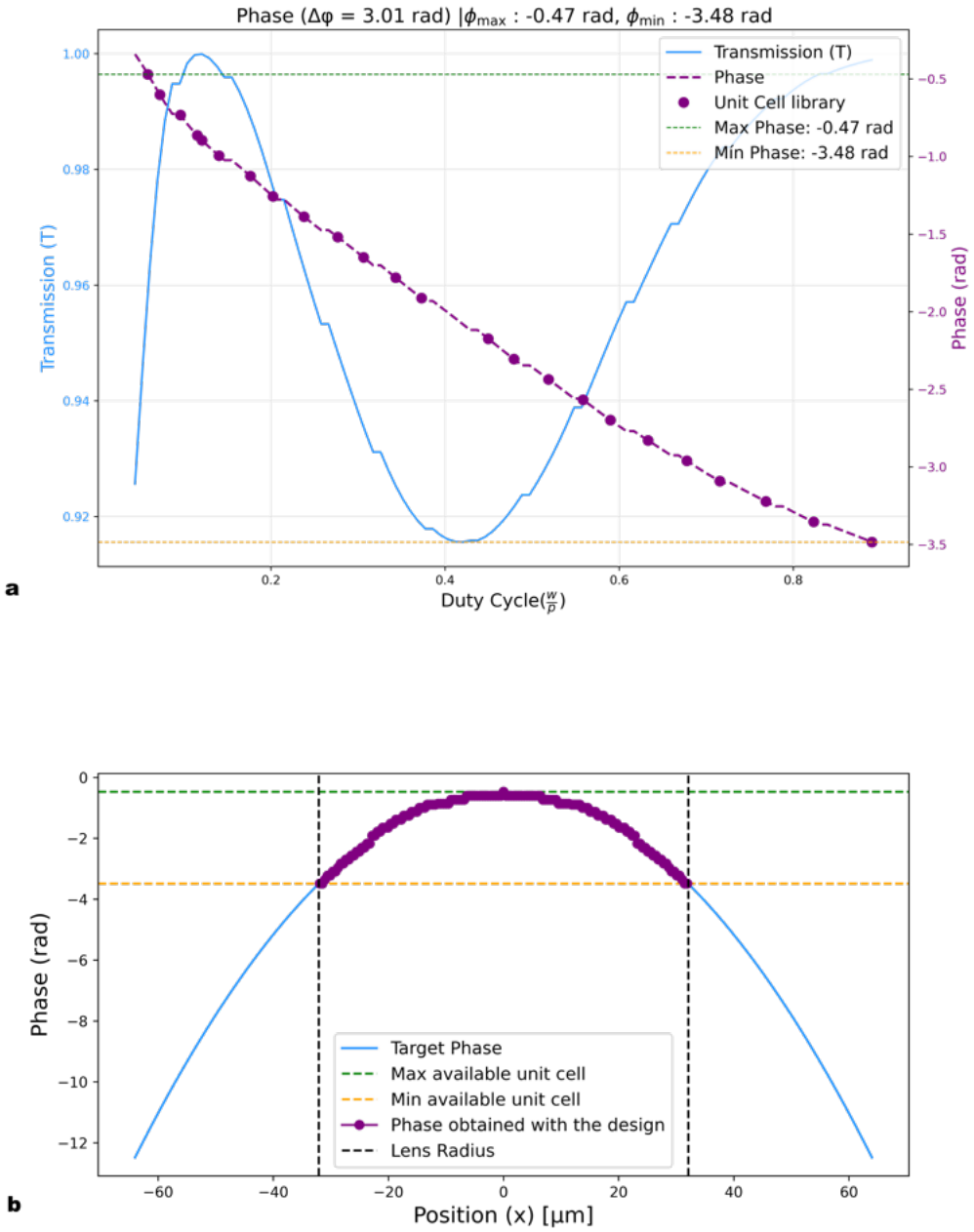

Figure 4.2: Metalens Design: Unit-Cell Selection and Phase Profile. **(a)** Interpolated transmission $T(dc)$ and phase $\phi(dc)$ as a function of the unit-cell diameter dc for optimized design parameters (period $p = 0.456\,\mu$m and thickness $t = 0.583\ \mu$m). The purple dots are the unit-cells that are selected for the unit-cell library. **(b)** The resulting full-lens phase distribution for a target focal length of $f = 1000\ \mu$m. This figure illustrates the application of the selected unit-cells to realize the required spherical phase profile across the lens aperture. The orange and green line mark the limits of the phase reach and therefore also mark the diameter of the lens.

In conclusion, the design method presented here allows the design of a metalens which has close to target focal distance. The design process began with an optimization scheme to determine the optimal (p, t) combination for the unit-cells, maximizing transmissivity (T) while ensuring sufficient phase coverage $(\Delta\phi > 0.8\pi)$. The selected parameters were $(p, t) = (0.456\ \mu$m, $0.583\ \mu$m) resulting in $T_{\text{min}} = 0.915$.

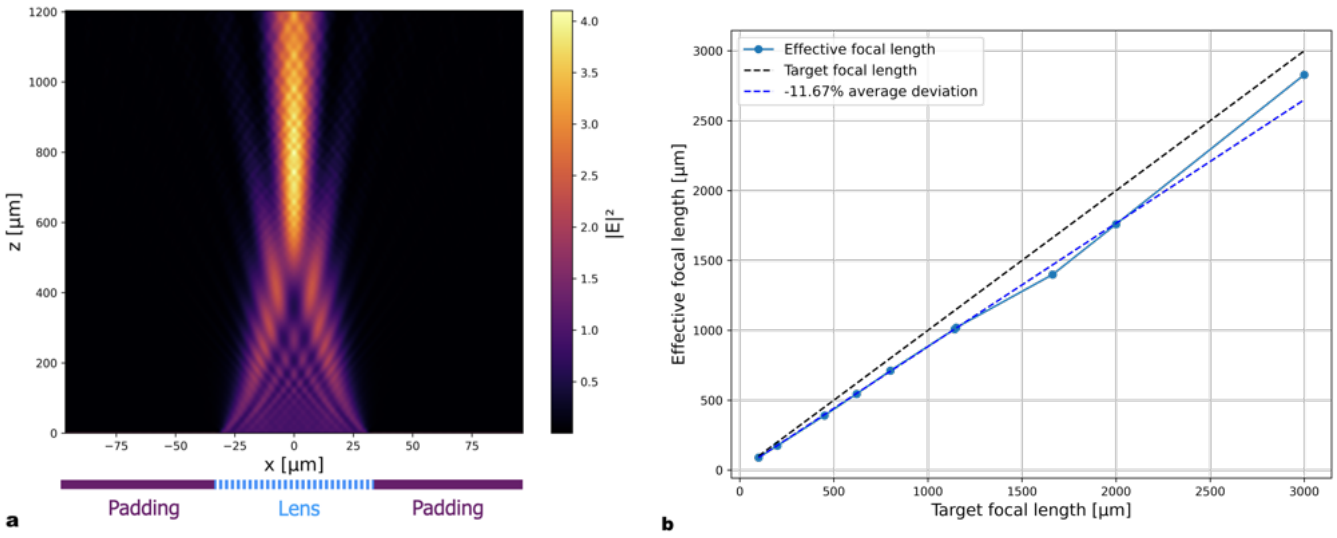

Figure 4.3: Metalens Design and Performance Evaluation. **(a)** Illustration of a designed Metalens with surrounding padding. **(b)** Comparison between the target focal length (used in the design) and the effective focal length (obtained from full-lens RCWA simulations). The dashed black line indicates the ideal one-to-one correspondence. The dashed blue line, representing the simulated effective focal length, deviates significantly by an average of 11.7% from the initial design value.

Subsequently, a unit-cell library was constructed resulting in a phase reach of $\Delta\phi = 3.01$ rad $\approx 0.96\pi$ (Figure 4.2a). This limited phase reach, however, constrained the diameter of the initial lens designs, resulting in a relatively high average focal length deviation of 11.7% (Figure 4.3b). This limitation also meant that the required minimum NA of ≈ 0.86 ($\theta_{\max} \approx 59°$) for generating the OPF could not be reached.
To overcome the diameter constraint, the wrapped-phase approach was implemented, enabling the construction of larger metalenses by periodically mapping the target phase to the available phase bins. This method significantly improved the simulation accuracy, reducing the average focal length deviation to a low 2.88% (Figure 4.4c). This focal length error is competitive for metalens design as most focal lengths deviations in literature fall between 1% and 10% [36]
This confirmed that the combination of high transmissivity (maximizing light throughput) and the truncated phase approach (maximizing lens diameter and NA) successfully satisfies the design requirements. The increased lens size allows for the achievement of the high Numerical Aperture necessary to satisfy the condition for the generation of the optical pulling force.

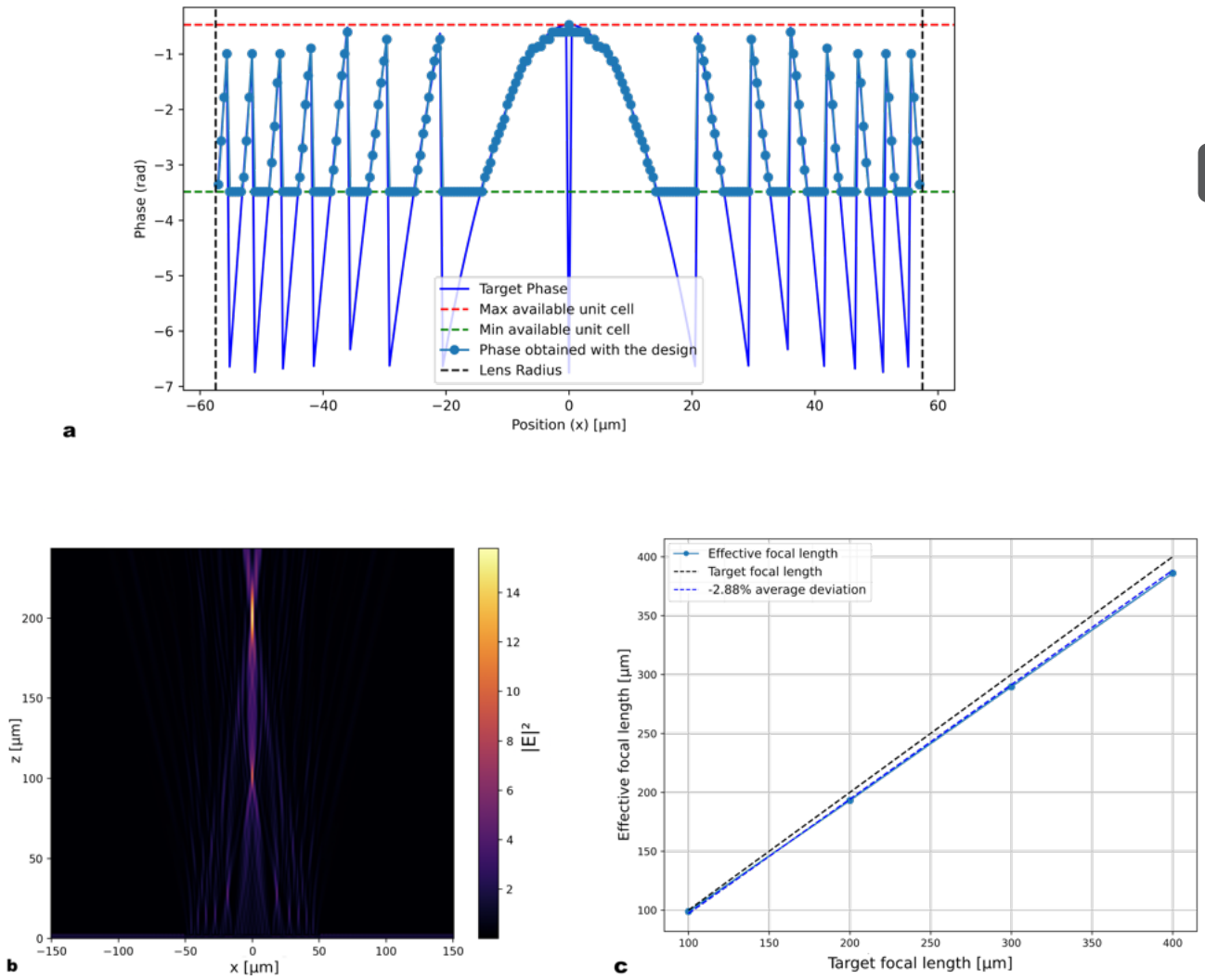

Figure 4.4: Analysis of Truncated Metalenses. **(a)** Truncated phase profile for a target focal length of 200 μm. The wrapped-phase approach enables the construction of a larger lens (here up to 60 μm diameter), surpassing the previous limitation of ≈ 30 μm imposed by the unit-cell library. **(b)** Electric field distribution for the truncated lens with a target focal length of 200 μm. The left panel shows the computed electric-field intensity in the $x-z$ plane, illustrating the focusing behavior. The right panel displays the on-axis field profile, where the measured focal point $f_{\text{eff}} = 201.14$ μm demonstrates a close match to the target value even with flat regions in the phase profile. **(c)** Focal-length sweep for the truncated designs extended to 130% of the initial radius. The significantly smaller deviation from the target focal length indicates that increasing the lens diameter improves the accuracy of the realized focal point.

4.3. WORKFLOW FOR METALENS DESIGN FOR OPTICAL PULLING FORCES

In this project, a workflow to design and simulate metalenses for optical pulling forces was elaborated. In order to clarify and visualize this process Figure. 4.5 shows a flowchart of the process.

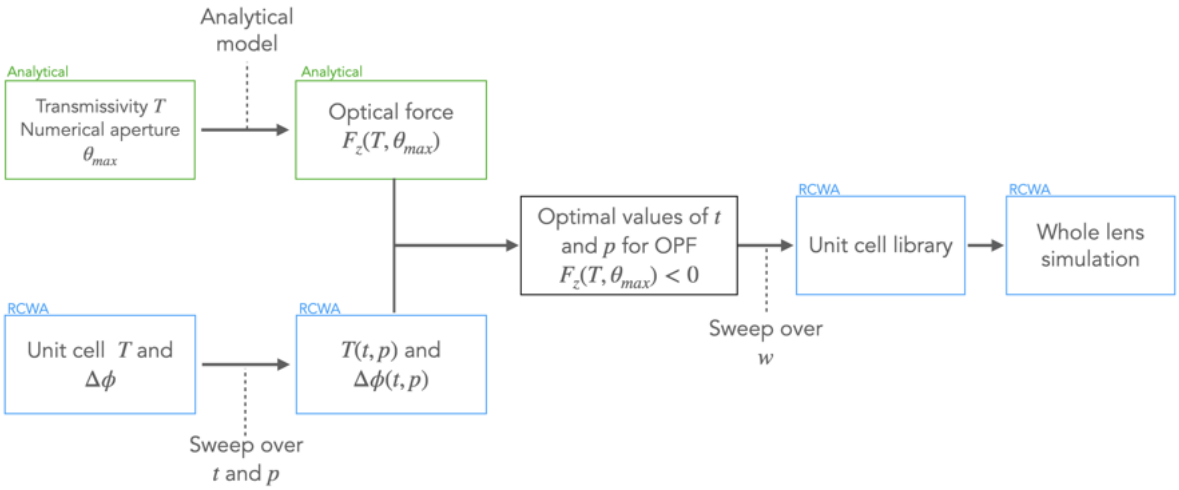

Figure 4.5: Workflow of the tractor-beam metalens design process. In the green rectangles are the parts of the process determined analytically and in blue the parts of the process determined by RCWA simulation. $\tan\theta_{\max} = \left(D/2f\right) = \sin^{-1}(\text{NA})$ defines the dimensions of the system, p is the period of the lens, t is the thickness, w is the width of the slits of the unit-cells T is the transmissivity of the unit-cells, $\Delta\phi$ is the phase maximum phase reach of the created metalens.

The workflow combines input from two main axes: the analytical formula for the optical force $F(T,\theta_{\max})$, and the simulated transmissivity and phase response of different thickness–period pairs (t,p). These two components are used together to identify optimal combinations of (t,p) that could enable an optical pulling force. This yields a transmissivity–phase map (constructed by sweeping over the slit width w of the unit-cell), which in turn guides the placement of unit-cells across the aperture and enables full-lens simulations.
This workflow can be adapted and repeated for new systems. It can therefore be extended to include practical fabrication considerations such as introducing a substrate layer, enforcing minimum feature sizes, or accounting for etch-depth variability, thereby bringing the design process closer to manufacturable.

5

LEVITATION OF THE METALENS

5.1. CONTEXTUALIZATION OF THE OPTICAL PULLING FORCE

This final Chapter evaluates the practical feasibility of using the designed metalens to generate a sufficient optical pulling force to levitate the lens against its own gravitational weight. This analysis translates the theoretical OPF requirements into measurable physical parameters, specifically the required laser power density.

Based on equation 3.5, the optical pulling force per unit length can be written as:

$$F_{z,\text{tot}} = \frac{2P}{c}\left(\sin\theta_{\max} + \theta_{\max}(1-2T)\right), \tag{5.1}$$

where P is now the incident linear power density (W/m)[1] . Substituting the characteristic parameters $T = 0.915$ and $\theta_{\max} = 1.039$ rad which are obtained from the parameter optimization in section 4.1 gives:

$$\begin{aligned} F_{z,\text{tot}} &= \frac{2P}{c}\left(\sin 1.039 + 1.039(1-2\times 0.915)\right) \\ &= \frac{2P}{c} \times (-4.72\times 10^{-4})\ \frac{\text{N}}{\text{m}}, \end{aligned} \tag{5.2}$$

which shows that the generated pulling force scales linearly with the applied power density P, and corresponds to a momentum transfer efficiency on the order of $\frac{F_{z,\text{tot}}}{P} \approx 10^{-12}\,\text{N m/W}$. This order of magnitude matches the values from the work of Peng et al. [28] validating the analytical method and formula. To contextualize this optical force, the laser power needed in order to lift the lens against its own weight is analyzed. The gravitational weight of the lens is calculated using the lens thickness t, material density ρ, and the solid-to-air fill fraction (which was established as being 80% on average). The balance between the optical pulling force and the gravitational force was evaluated over illumination angles $\theta_{\max} \in [60°, 90°]$ as this is the interval in which the force is possibly negative (Chapter 3 and 4.1). For each parameter set, the net force on the lens is computed:

$$F_{\text{net}} = F_{\text{optical}} - F_{\text{gravity}}$$

where $F_{\text{net}} > 0$ indicates a net pulling force in the direction opposite to the gravitational acceleration.
Figure 5.1b shows the parameters (green dots) for which the total force experienced by the lens is negative, meaning that the pulling force manages to take over the gravitational pull. It is visible here that the power needed to obtain this is quite elevated and that setups with lower focal points are favorable to lifting the lens against its own weight.

In Figure 5.1c the net force for a certain focal distance is shown, the continuous white line represents the

[1] All forces and masses are expressed *per unit length* in the invariant direction of the one-dimensional metalens. In this configuration, the lens is considered translationally invariant along the y-axis (the slit direction), and all quantities are therefore evaluated per meter in y. Consequently, the incident optical power is treated as a *linear power density* (W/m) rather than a total power. This ensures that both the resulting optical force and the gravitational weight are expressed consistently in N/m. The computed values are therefore relative to the extent of the lens in the invariant y-direction; to obtain absolute forces for a lens of finite width, these quantities can be multiplied by the actual dimension of the device in y.

frontier point between a net negative force and a positive force. Notably, the relation between the required power for lift and the numerical aperture (NA), represented by the angle θ_{max}, is not linear ie. there is a minimal power which allows levitation showed by the dotted line. This minimum is plotted for a range of focal lengths in Figure 5.1d. The data exhibit a linear dependence between $\log_{10}(P_{min})$ and $\log_{10}(f)$, indicating a power-law relation of the form $P_{min} \propto f^n$,.

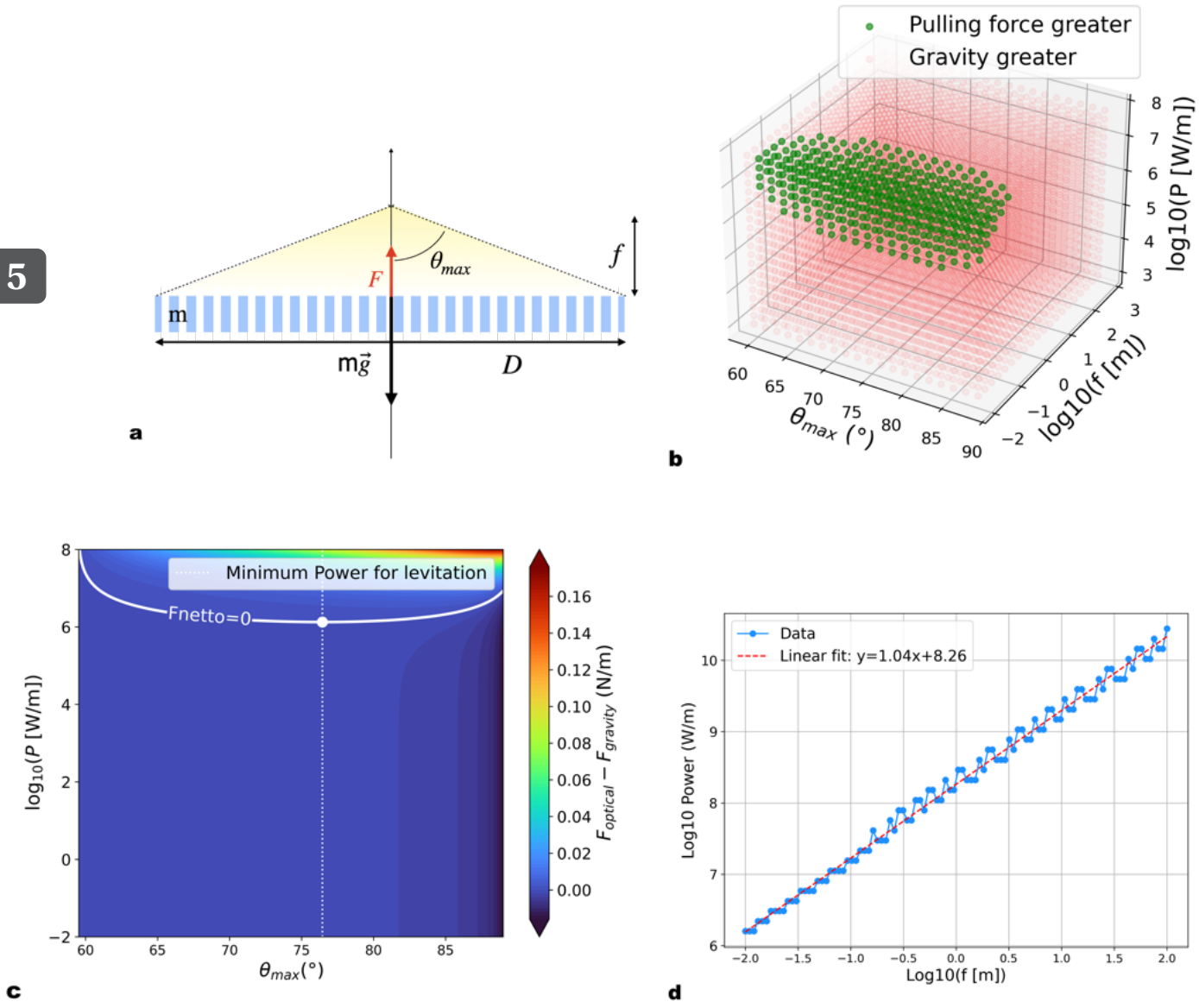

Figure 5.1: Analysis of OPF Feasibility, Power Scaling, and Geometric Parameters. **(a)** Schematic defining the geometric and force parameters (D, f, t, m, F, $\vec{g}$, θ_{max}) for the 1-D metalens. **(b)** 3D scatter plot illustrating the levitation feasibility across focal length, incident angle, and power density. **(c)** Contour map of the net optical force (F_{net}) for $f = 0.01$ m, where the $F_{net} = 0$ condition shows the required power threshold for levitation. **(d)** Minimum incident power density (P_{min}) required to balance the gravitational weight versus focal length (f), confirming a $P_{min} \propto f^n$ power-law dependence. The required minimum power angle was constant at $\theta = 76.5°$.

When evaluating the feasibility of lifting a metalens against its own weight, it is instructive to compare the required dimensions and optical power with experimentally demonstrated limits in optical levitation. In the

work by Arita *et al.* [37], a microparticle of about 10 μm is optically trapped in vacuum and used to detect rotation rates.
For a metalens of comparable diameter (10 μm) and an illumination angle of $\theta = 76.49°$, the linear fit in Fig. 5.1d predicts a required focal power density on the order of $10^{2.5}$ W/m with a focal distance of 3 μm. Assuming the lens extends equally in both the invariant and variant directions, this corresponds to a total optical power of approximately 0.32 mW at the working wavelength of 1.070 μm. This is lower than the power of 25 mW used in the literature. This comparison highlights that the power required to levitate a microstructured metalens of similar size is of the same order of magnitude as that used in state-of-the-art optical trapping experiments. The lower power is encouraging because it suggests lower absorption induced heating and thereby widen the range of possible applications. For instance, on of the complications of carrying out in vivo optical traps is related to the use of high power which causes issues like photodamage [38].
Using the same approximation method, it can be determined that using a 1.070 μm laser with 400 W of power (available at the Norte Lab), a metalens of diameter $D \approx 3$ mm could be levitated at a distance $f \approx 0.93$ mm from the laser.
This suggests that optical pulling of lightweight metasurfaces lies within experimentally accessible power ranges. Further optimization of the lens geometry and transmission efficiency could therefore bring practical levitation conditions even closer to those demonstrated in optical trapping of microscopic objects.

5.2. IMPROVEMENTS AND RECOMMENDATIONS

ANALYTICAL MODEL

The theoretical model developed in this work provides a simple and intuitive description of the optical pulling force and its limiting dependencies. However, it neglects several physical effects that may become significant. In particular, the model treats the metalens as an infinite, uniform phase element and does not account for edge effects. In practice, the boundary of the lens may not match the footprint of the incident beam perfectly, and the redistribution of momentum at the edges could alter the net force. Investigating how different aperture shapes, truncation geometries, or beam–lens misalignment modify the pulling force would therefore be a valuable next step. Moreover, analyzing how stably the metalens can be levitated at its focal distance from the laser, considering both axial and lateral stability,would further clarify the practical feasibility of sustained optical levitation.

To further assess the validity of the theoretical model, one could compute Maxwell stress tensor [28] on small metalenses using the simulated electromagnetic field surrounding it. This would provide a more rigorous benchmark for the analytical predictions and clarify to what extent the model can be reliably used for design and manufacturability. Ultimately, MST evaluation on the full metalens would give a complete picture of the force distribution, including contributions from discontinuities introduced by the wrapping of the phase.

DESIGN WORKFLOW

Although the workflow (Fig. 4.5) is in principle scalable to arbitrarily large metalens diameters, the present study was restricted to lenses below a few hundred micrometres. This limitation arose from computational constraints. As described in Appendix D, the current RCWA supercell implementation becomes memory-limited on the personal computer used for the simulations, when determining the focal point of very large lenses. With improved computational resources, GPU acceleration, or more efficient code parallelization, the same workflow could be applied to metalenses approaching millimeter or even macroscale dimensions. However, assuming that the focal distances follow the trend set out in Figure.4.4c, the design approach itself is not computationally expensive and can be followed for larger lenses without the simulation of the focal point.

Finally, several practical aspects remain unexplored but important for eventual experimental realization. These include tolerance to fabrication errors (slit width, etch depth, and sidewall angle), the influence of material absorption at high optical powers, temperature rise under illumination, and the impact of realistic Gaussian beam quality and pointing stability. Incorporating these factors into future simulations and design iterations would significantly improve the manufacturability and robustness of the proposed metalens designs.

6

CONCLUSION

This study established theoretical limitations, optimized the design parameters, and evaluated the experimental feasibility of levitating a metalens using optical pulling forces .

The theoretical analysis provides a simple yet effective expression for the optical force on a metalens. Compared to full electromagnetic evaluation using the Maxwell stress tensor as performed, for instance, by Peng et al. [28], the analytical formula offers a computational advantage. For larger lenses, computing the full electric-field distribution required for MST evaluation becomes expensive, whereas the analytical expression enables fast estimation of the expected pulling force across a wide parameter space.
Furthermore, the analysis showed there were strict limits to the achievable OPF, which depends critically on the metalens's transmissivity. Achieving a net pulling force requires the force exerted by the high-angle light at the outer parts of the lens to compensate for the predominantly positive (pushing) force generated by the low-angle light at the center. This dependence defined two limiting factors on the OPF: the lens numerical aperture (NA) and the lens transmissivity.
The design phase was made to address these limits. An optimization scheme was used to select the optimal unit-cell parameters ((p, t) = (0.456 μm, 0.583 μm)) which yielded a high minimum transmissivity of $T_{\text{min}} = 0.915$. Although the initial unit-cell library had a limited phase reach ($\Delta\phi \approx 0.96\pi$), the implementation of the wrapped-phase approach allowed for the construction of larger metalenses. This scaling enabled the designs to achieve the high numerical aperture required by the OPF condition, while concurrently reducing the average focal length deviation in full-lens simulations from 11.7% to an accurate 2.88%.

Finally, the feasibility of levitation was assessed by balancing the optical pulling force against the lens's gravitational weight. The net force analysis confirmed that lower focal lengths and a specific range of illumination angles (60° to 90°) are favorable for achieving a net pulling force ($F_{\text{net}} > 0$). The minimum power required for levitation (P_{min}) exhibited a clear power-law dependence on the focal length, $P_{\text{min}} \propto f^{n}$.

In summary, this work provides a comprehensive design workflow that is presented in Figure.4.5 that satisfies the theoretical requirements for optical pulling force generation and demonstrates that the required optical power lies within experimentally accessible ranges, positioning lightweight metasurfaces as promising candidates for advanced non-contact manipulation and levitation.

REFERENCES

[1] C. Gonzalez-Ballestero, M. Aspelmeyer, L. Novotny, R. Quidant en O. Romero-Isart, "Levitodynamics: Levitation and control of microscopic objects in vacuum," *Science*, jrg. 374, nr. 6564, okt 2021. DOI: 10.1126/science.abg3027.

[2] Y. Jin, K. Shen, P. Ju en T. Li, *Towards real-world applications of levitated optomechanics*, jul 2024.

[3] T. Liang e.a., "Yoctonewton force detection based on optically levitated oscillator," *Fundamental Research*, jrg. 3, nr. 1, p. 57–62, jan 2023. DOI: 10.1016/j.fmre.2022.09.021.

[4] J. Ahn, Z. Xu, J. Bang, P. Ju, X. Gao en T. Li, "Ultrasensitive torque detection with an optically levitated nanorotor," *Nature Nanotechnology*, jrg. 15, nr. 2, p. 89–93, feb 2020, Publisher: Nature Publishing Group. DOI: 10.1038/s41565-019-0605-9.

[5] J. Bang e.a., "Five-dimensional cooling and nonlinear dynamics of an optically levitated nanodumbbell," *Physical Review Research*, jrg. 2, nr. 4, p. 043 054, okt 2020, Publisher: American Physical Society. DOI: 10.1103/PhysRevResearch.2.043054.

[6] H. Pi e.a., "Levitation and controlled MHz rotation of a nanofabricated rod by a high-NA metalens," *Microsystems & Nanoengineering*, jrg. 11, nr. 1, p. 67, apr 2025, Publisher: Nature Publishing Group. DOI: 10.1038/s41378-025-00886-7.

[7] L. Norder e.a., "Pentagonal photonic crystal mirrors: scalable lightsails with enhanced acceleration via neural topology optimization," *Nature Communications*, jrg. 16, nr. 1, p. 2753, mrt 2025, Publisher: Nature Publishing Group. DOI: 10.1038/s41467-025-57749-y.

[8] L. Michaeli e.a., "Direct radiation pressure measurements for lightsail membranes," *Nature Photonics*, jrg. 19, nr. 4, p. 369–377, apr 2025, Publisher: Nature Publishing Group. DOI: 10.1038/s41566-024-01605-w.

[9] J. Guo, R. A. Norte en S. Gröblacher, "Integrated optical force sensors using focusing photonic crystal arrays," *Optics Express*, jrg. 25, nr. 8, p. 9196–9203, apr 2017, Publisher: Optica Publishing Group. DOI: 10.1364/OE.25.009196.

[10] L. Lialys, J. Lialys, A. Salandrino, B. D. Ackley en S. Fardad, "Optical trapping of sub-millimeter sized particles and microorganisms," *Scientific Reports*, jrg. 13, nr. 1, p. 8615, mei 2023, Publisher: Nature Publishing Group. DOI: 10.1038/s41598-023-35829-7.

[11] N. Carlon Zambon e.a., "Motional entanglement of remote optically levitated nanoparticles," *Physical Review A*, jrg. 111, nr. 1, p. 013 521, jan 2025, Publisher: American Physical Society. DOI: 10.1103/PhysRevA.111.013521.

[12] S. Sukhov en A. Dogariu, "On the concept of "tractor beams"," *Optics Letters*, jrg. 35, nr. 22, p. 3847, nov 2010. DOI: 10.1364/OL.35.003847.

[13] H. Li e.a., "Optical pulling forces and their applications," *Advances in Optics and Photonics*, jrg. 12, nr. 2, p. 288, jun 2020. DOI: 10.1364/AOP.378390.

[14] V. G. Shvedov, A. S. Desyatnikov, A. V. Rode, W. Krolikowski en Y. S. Kivshar, "Optical guiding of absorbing nanoclusters in air," *Optics Express*, jrg. 17, nr. 7, p. 5743–5757, mrt 2009, Publisher: Optica Publishing Group. DOI: 10.1364/OE.17.005743.

[15] Y. Shi e.a., "Nanometer-precision linear sorting with synchronized optofluidic dual barriers," *Science Advances*, jrg. 4, nr. 1, eaao0773, jan 2018, Publisher: American Association for the Advancement of Science. DOI: 10.1126/sciadv.aao0773.

[16] J. Durnin, J. J. Miceli en J. H. Eberly, "Diffraction-free beams," *Physical Review Letters*, jrg. 58, nr. 15, p. 1499–1501, apr 1987, Publisher: American Physical Society. DOI: 10.1103/PhysRevLett.58.1499.

[17] W. Ding, T. Zhu, L.-M. Zhou en C.-W. Qiu, "Photonic tractor beams: a review," *Advanced Photonics*, jrg. 1, nr. 2, p. 024 001, mrt 2019, Publisher: SPIE. DOI: 10.1117/1.AP.1.2.024001.

[18] A. Mizrahi en Y. Fainman, "Negative radiation pressure on gain medium structures," *Optics Letters*, jrg. 35, nr. 20, p. 3405, okt 2010. DOI: 10.1364/OL.35.003405.

[19] K. J. Webb en Shivanand, "Negative electromagnetic plane-wave force in gain media," *Physical Review E*, jrg. 84, nr. 5, p. 057 602, nov 2011. DOI: 10.1103/PhysRevE.84.057602.

[20] Q. Sun, K. Dholakia en A. D. Greentree, "Optical Forces and Torques on Eccentric Nanoscale Core–Shell Particles," *ACS Photonics*, jrg. 8, nr. 4, p. 1103–1111, apr 2021. DOI: 10.1021/acsphotonics.0c01825.

[21] A. Dogariu, S. Sukhov en J. Sáenz, "Optically induced 'negative forces'," *Nature Photonics*, jrg. 7, nr. 1, p. 24–27, jan 2013, Publisher: Nature Publishing Group. DOI: 10.1038/nphoton.2012.315.

[22] S. Sukhov en A. Dogariu, "Negative Nonconservative Forces: Optical "Tractor Beams" for Arbitrary Objects," *Physical Review Letters*, jrg. 107, nr. 20, p. 203 602, nov 2011. DOI: 10.1103/PhysRevLett.107.203602.

[23] M. Pan e.a., "Dielectric metalens for miniaturized imaging systems: progress and challenges," *Light: Science & Applications*, jrg. 11, nr. 1, p. 195, jun 2022, Publisher: Nature Publishing Group. DOI: 10.1038/s41377-022-00885-7.

[24] F. Lu, F. G. Sedgwick, V. Karagodsky, C. Chase en C. J. Chang-Hasnain, "Planar high-numerical-aperture low-loss focusing reflectors and lenses using subwavelength high contrast gratings," *Optics Express*, jrg. 18, nr. 12, p. 12 606, jun 2010. DOI: 10.1364/OE.18.012606.

[25] D. Fattal, J. Li, Z. Peng, M. Fiorentino en R. G. Beausoleil, "Flat dielectric grating reflectors with focusing abilities," *Nature Photonics*, jrg. 4, nr. 7, p. 466–470, jul 2010, Publisher: Nature Publishing Group. DOI: 10.1038/nphoton.2010.116.

[26] H. A. Atwater e.a., "Materials challenges for the Starshot lightsail," *Nature Materials*, jrg. 17, nr. 10, p. 861–867, okt 2018, Publisher: Nature Publishing Group. DOI: 10.1038/s41563-018-0075-8.

[27] A. R. Agrawal, J. Manley, D. Allepuz-Requena en D. J. Wilson, "Focusing membrane metamirrors for integrated cavity optomechanics," *Optica*, jrg. 11, nr. 9, p. 1235, sep 2024. DOI: 10.1364/OPTICA.522509.

[28] M. Peng e.a., "Optical Pulling Using Chiral Metalens as a Photonic Probe," *Nanomaterials*, jrg. 11, nr. 12, p. 3376, dec 2021, Number: 12 Publisher: Multidisciplinary Digital Publishing Institute. DOI: 10.3390/nano11123376.

[29] A. B. Klemm e.a., "Experimental high numerical aperture focusing with high contrast gratings," *Optics Letters*, jrg. 38, nr. 17, p. 3410–3413, sep 2013, Publisher: Optica Publishing Group. DOI: 10.1364/OL.38.003410.

[30] A. Zhan, S. Colburn, R. Trivedi, T. K. Fryett, C. M. Dodson en A. Majumdar, "Low-Contrast Dielectric Metasurface Optics," *ACS Photonics*, jrg. 3, nr. 2, p. 209–214, feb 2016, Publisher: American Chemical Society. DOI: 10.1021/acsphotonics.5b00660.

[31] P. Lalanne, S. Astilean, P. Chavel, E. Cambril en H. Launois, "Blazed binary subwavelength gratings with efficiencies larger than those of conventional échelette gratings," *Optics Letters*, jrg. 23, nr. 14, p. 1081–1083, jul 1998, Publisher: Optica Publishing Group. DOI: 10.1364/OL.23.001081.

[32] R. Baets e.a., "Silicon Photonics: silicon nitride versus silicon-on-insulator," in *Optical Fiber Communication Conference (2016), paper Th3J.1*, Optica Publishing Group, mrt 2016, Th3J.1. DOI: 10.1364/OFC.2016.Th3J.1.

[33] Y. He, B. Song en J. Tang, "Optical metalenses: fundamentals, dispersion manipulation, and applications," *Frontiers of Optoelectronics*, jrg. 15, nr. 1, p. 24, mei 2022. DOI: 10.1007/s12200-022-00017-4.

[34] M. G. Moharam en T. K. Gaylord, "Rigorous coupled-wave analysis of planar-grating diffraction," *JOSA*, jrg. 71, nr. 7, p. 811–818, jul 1981, Publisher: Optica Publishing Group. DOI: 10.1364/JOSA.71.000811.

[35] Y.-J. L. Chu, E. M. Jansson en G. A. Swartzlander, "Measurements of Radiation Pressure Owing to the Grating Momentum," *Physical Review Letters*, jrg. 121, nr. 6, p. 063 903, aug 2018, Publisher: American Physical Society. DOI: 10.1103/PhysRevLett.121.063903.

[36] R. Liu, L. Li en J. Zhou, "The Principle and Application of Achromatic Metalens," *Micromachines*, jrg. 16, nr. 6, p. 660, mei 2025. DOI: 10.3390/mi16060660.

[37] Y. Arita, M. Mazilu en K. Dholakia, "Laser-induced rotation and cooling of a trapped microgyroscope in vacuum," *Nature Communications*, jrg. 4, nr. 1, p. 2374, aug 2013, Publisher: Nature Publishing Group. DOI: 10.1038/ncomms3374.

[38] I. A. Favre-Bulle, A. B. Stilgoe, E. K. Scott en H. Rubinsztein-Dunlop, "Optical trapping in vivo: theory, practice, and applications," *Nanophotonics*, jrg. 8, nr. 6, p. 1023–1040, jun 2019, Publisher: De Gruyter. DOI: 10.1515/nanoph-2019-0055.

[39] R. C. Rumpf, "Improved formulation of scattering matrices for semi-analytical methods consistent with standard conventions," *Progress In Electromagnetics Research B*, jrg. 35, p. 241–261, 2011. DOI: 10.2528/PIERB11083107.

[40] W. Jin, W. Li, M. Orenstein en S. Fan, "Inverse Design of Lightweight Broadband Reflector for Relativistic Lightsail Propulsion," *ACS Photonics*, jrg. 7, nr. 9, p. 2350–2355, sep 2020, Publisher: American Chemical Society. DOI: 10.1021/acsphotonics.0c00768.

A

RCWA AS A SIMULATION METHOD

In this work, rigorous coupled-wave analysis (RCWA) [34] is used to compute the transmission amplitude and phase transformation of a periodic crystal structure. This computational method is employed because it enables fast and accurate analysis of periodic electromagnetic structures. In RCWA, the structure is divided into layers that are stacked along the z-direction, while the pattern, or unit-cell, repeats periodically in the x and y directions. Within each layer, Maxwell's equations are solved, with boundary conditions determined by the fields in the layers above and below. In the x and y directions, periodic boundary conditions are applied. The entire multilayer stack of N layers is described by the Redheffer star product of the individual scattering matrices,

$$S = S^{(1)} \otimes S^{(2)} \otimes \cdots \otimes S^{(N)}, \tag{A.1}$$

where the individual scattering matrices $S^{(i)}$ are defined following the formulation of Raymond Rumpf in [39]. The global scattering matrix connects the input and output field coefficients as

$$\begin{bmatrix} a_N \\ b_0 \end{bmatrix} = S \begin{bmatrix} a_0 \\ b_N \end{bmatrix}, \tag{A.2}$$

where a_0 are the forward incident amplitudes (known input), b_0 the reflected amplitudes (output), a_N the transmitted amplitudes (output), and b_N the backward amplitudes in the substrate (usually 0 for a semi-infinite substrate). The relation between the coefficients in successive layers is given by

$$\begin{bmatrix} a_i \\ b_{i-1} \end{bmatrix} = \begin{bmatrix} S_{11}^{(i)} & S_{12}^{(i)} \\ S_{21}^{(i)} & S_{22}^{(i)} \end{bmatrix} \begin{bmatrix} a_{i-1} \\ b_i \end{bmatrix} = S^{(i)} \begin{bmatrix} a_{i-1} \\ b_i \end{bmatrix}, \tag{A.3}$$

where a_{i-1} and b_i represent the incoming waves from the top and bottom, respectively (see Fig. **??**), and $S^{(i)}$ is the i-th local scattering matrix. The local electric field within the ith layer is given by

$$E_{\parallel}(z) = e^{ik_0\Omega(z-z_i)}\, a_i + e^{-ik_0\Omega(z-z_{i+1})}\, b_i, \tag{A.4}$$

where $E_{\parallel}(z) = [E_x(z) \;\; E_y(z)]^T$ is the tangential electric field inside layer i, a_i are the forward-propagating mode amplitudes at the top of layer i, b_i are the backward-propagating mode amplitudes at the bottom of layer i, Ω is the diagonal matrix containing the normalized z-components of the propagation constants, z_i and z_{i+1} are the z-positions of the top and bottom interfaces of layer i, respectively, and $k_0 = 2\pi/\lambda$ is the free-space wavenumber. The `gRCWA` package [40] computes the scattering matrices of the multilayer structure, which allows the extraction of the forward- and backward-propagating mode amplitudes. From these relations, the mode amplitudes within each layer can be reconstructed at any vertical position z. The overall transmission and reflection properties of the stack follow directly from the amplitudes at the first and last interfaces: the transmitted field corresponds to the forward-propagating amplitudes a_N in the substrate, while the incident field is represented by a_i in the first layer. In practice, `gRCWA` retrieves these quantities through the function `GetAmplitudes`, for example:

```
ai, bi = obj.GetAmplitudes(which_layer, z_offset)
```

The transmission phase of the zeroth diffraction order is determined from the phase difference between the incident forward-propagating coefficient and the forward-propagating coefficient transmitted through the sample. While the transmissivity of the sample can be directly extracted using the `RT_Solve` function, which computes the reflection and transmission coefficients of the entire multilayer stack based on the global scattering matrix, this output only provides the magnitude information; the phase must be obtained from the complex modal amplitudes.

B

DERIVATION OF THE OPTICAL FORCE ON THE LENS

To describe the conditions under which a metalens can generate an optical pulling force, one can start from the momentum conservation law for the incident, reflected, and transmitted fields [22][35]. Consider a light ray incoming at an incident angle θ_i on a grating locally considered as periodic. The conservation of momentum can be expressed as:

$$\vec{k}_{\text{grating}} = \sum_m \vec{k}_{r,m} + \vec{k}_i + \vec{k}_t \tag{B.1}$$

where $\vec{k_i}$ ($\vec{k_t}$) is the incident (transmitted) wave vector as depicted in figure, the transmitted wave vector and $\vec{k_{r,m}}$ the reflection into multiple diffraction orders. The wave vectors are schematized in figure 3.1. For every incident angle θ_i the force on the grating becomes [35]

$$\vec{F}_i = \frac{P_i}{ck}\left(\vec{k}_i - \sum_m \eta_m \vec{k}_{r,m}\right), \quad \text{where } |\vec{k}_i| = |\vec{k}_t| = |\vec{k}_{r,m}| = k = \frac{2\pi}{\lambda} \tag{B.2}$$

with $\eta_m = \frac{P_m}{P_i}$ the efficiency of the reflected orders (such that $\sum_m \eta_m = 1$); P_i (P_m) si the incident beam power and c the speed of light. Assuming transmitted beams are collimated parallel to the optical axis by the design of the lens, the projection on the z axis is taken

$$F_z(\theta_i) = \frac{P_i}{c}\left(\cos\theta_i - \frac{P_t}{P_i} + \sum_m \frac{P_m}{P_i}\cos\theta_{rm}\right). \tag{B.3}$$

The Transmission and Reflection are defined in the following way (to correspond to the RCWA definition)

$$T = \frac{\sum_m P_m^{\text{trans}}}{P_i} \qquad R = \frac{\sum_m P_m^{\text{ref}}}{P_i} \tag{B.4}$$

which concludes the equation for the force generated by shining a ray with an incidence angle on a locally periodic grating:

$$F_z(\theta_i) = \frac{P_i}{c}\left(\cos\theta_i - T + \sum_m R_m \cos\theta_{rm}\right). \tag{B.5}$$

The pulling force is lowest when the pushing force is maximal, which happens when the reflection for all orders is normal ($\theta_{r,m} = 0$). Then, with $\sum R_m = (1-T)$ (assuming no absorption), the formula for the force can be simplified to a version in the worst case scenario (normal reflection), which should lead to an estimate of the lowest pulling force achievable:

$$F_z(\theta_i) = \frac{P_i}{c}\left(\cos\theta_i - 2T + 1\right). \tag{B.6}$$

This work aims to use an incident diverging light beam. A diverging light beam is constituted by a sum of plane waves with, varying incident angles θ_i, which all contribute differently to the force along z. A plane

wave with normal incidence ($\theta_i = 0$) can only create a pushing force (see chapter) while waves with parallel incidence ($\theta_i = \pi/2$) contribute the most effectively to to the negative force. Obviously, there should exists an angle of incidence $0 < \theta_{\min} < \pi/2$ at which the pushing and pulling force negate and the plane wave contribution to the negative force is zero [22]. Therefore there is only a negative force on the parts of the lens where $\theta_i > \theta_{\min}$. To estimate $\theta_{\min}$ the formula of the force is set to zero:

$$\begin{aligned} F_z(\theta_{\min}) &= 0 \\ \cos\theta_{\min} &= 2T - 1 \end{aligned} \tag{B.7}$$

Giving an estimate for the minimum angle of the negative force $\theta_{\min} = \cos^{-1}(2T-1)$ this is schematized in figure 3.2. The total force exerted on the lens is given by the sum over all angles of the diverging beam. Defining $\theta_{\max} = \tan^{-1}\left(\frac{D}{2f}\right)$ as the largest angle of the diverging beam as plotted in 3.2, related to the numerical aperture of the system by $\mathrm{NA} = \sin(\theta_{\max})$ the total sum can be written:

$$\begin{aligned} F_{z,\mathrm{tot}} &= \int_{-\theta_{\max}}^{\theta_{\max}} F_z(\theta_i)\,\mathrm{d}\theta_i \\ &= 2\underbrace{\int_0^{\theta_{\min}} F_z(\theta_i)\,\mathrm{d}\theta_i}_{\text{positive contribution}} + 2\underbrace{\int_{\theta_{\min}}^{\theta_{\max}} F_z(\theta_i)\,\mathrm{d}\theta_i}_{\text{negative contribution}} \end{aligned} \tag{B.8}$$

The negative force generated on the outside of the lens (where $\theta_i > \theta_{\min}$) needs to counteract the positive force at the inside of the lens (where $\theta_i < \theta_{\min}$). Assuming $P_i = P$ is constant across the angle interval

$$F_{z,\mathrm{tot}} = \frac{2P}{c}\left(\sin\theta_{\max} + \theta_{\max}(1-2T)\right) = \frac{2P}{c}\left(\mathrm{NA} + \sin^{-1}(\mathrm{NA})(1-2T)\right) \tag{B.9}$$

C

OPTIMIZATION OF THE THICKNESS AND PERIOD OF THE LENS

Before constructing the unit-cell library, several parameters are fixed within the workflow. The procedure used to optimize these parameters is detailed in this appendix.
The transmissivity of a unit-cell is dictated by period, thickness and width of the slit. The in–plane period p (center–to–center spacing between adjacent unit-cells) is bounded by two practical considerations. First, fabrication imposes a minimum space between slits of ≈ 50 nm, which we enforce as $p - w > 50$ nm, ensuring that that for any chosen period p the slit width w remains fabricable. Second, to achieve diffraction–limited focusing and maintain quasi-adiabatic variation of the unit-cells across the aperture (mitigating inter-cell coupling artifacts), the sampling criterion $p < \frac{\lambda}{2\mathrm{NA}}$ must be satisfied [33]. These two constraints provide, respectively, a lower and upper bound for and upper bound for p.

In order to identify a thickness that provides both high transmissivity and a wide phase range, an initial sweep over the membrane thickness was performed for a set period. Theminimumm transmission and phase response were evaluated for an interval of thicknesses of parameters for each duty cycle (dc). The results of this sweep are shown in Figure C.1. From these simulations, it became apparent that there is a trade-off between the transmissivity of a unit-cell and the phase transformation that the unit-cells are able to impart. As the larger the thickness is the more phase delay is possible but he lower the tranmissivity gets.
Consequently, thinner slabs are unable to accumulate a full 2π phase shift, limiting the available phase range. At the same time, the transmission exhibits a periodic variation with thickness, which can be attributed to interference inside the slab: the constructive interference condition is periodic in the optical path length $2nt = m\lambda$.

To determine the most favorable combination of unit-cell period p and slab thickness t, the transmissivity and phase responses were evaluated for each parameter pair over all duty cycles dc. The resulting sweeps were analyzed to identify the optimal (p, t) combination that satisfies the physical constraint given by 3.5. Each candidate pair was optimized according to the following criteria:

- **Phase coverage:** satisfy a minimum phase span of $\Delta\phi > 0.8\pi$. This threshold corresponds to the smallest phase transformation reported in literature that still enables the realization of a focusing grating, ensuring that the unit-cell library provides sufficient phase coverage.
- **Pulling-force condition:** minimize the implied propagation angle $\theta_{\max}$, such that the overall lens dimensions (diameter and focal length) remain within practical bounds while fulfilling the transmissivity constraint associated with a negative net axial force ($F_z < 0$), which equates to satisfying

$$T \geq T_\theta^{\min} = \frac{1}{2}\left(1 + \frac{\sin\theta}{\theta}\right), \tag{C.1}$$

  where $T_\theta^{\min}$ represents the minimum transmission required to achieve a net pulling force for a given propagation angle θ.

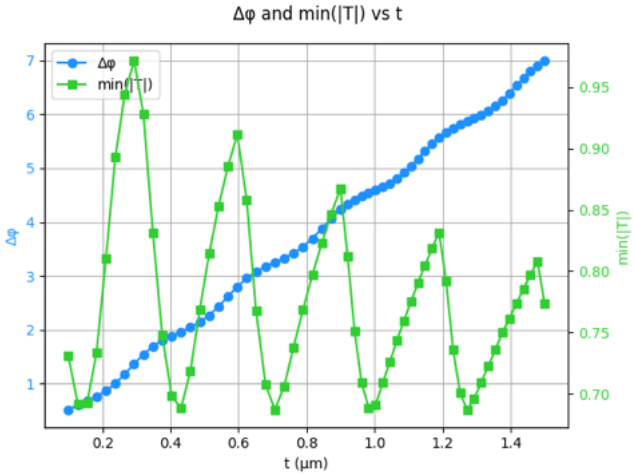

Figure C.1: A trade-off appears between high transmission (orange) and large achievable phase range (blue), originating from optical path length and interference in the membrane for period 0.250 um

Among all points satisfying both conditions ($F_z < 0$ and $\Delta\phi \geq 0.8\pi$), the pair (p, t) minimizing $\theta_{\max}$ was selected as optimal. For each period thickness pair (p, t), the minimum transmission, the phase span, and the implied minimum angle $\theta_{\max}(T)$ were computed. Only points fulfilling $\Delta\phi \geq 0.8\pi$ and $T \geq 0.85$ were retained for analysis. The optimization procedure described above produced a set of maps that illustrate how the optical performance of the unit-cells evolves with both period p and thickness t. Figures 4.1 display the transmission and phase-span distributions, while Figure 4.1(b) summarizes the trade-off between these two quantities through a Pareto representation. The optimal point $(p^*, t^*) = (0.456\ \mu\text{m}, 0.583\ \mu\text{m})$ corresponds to the geometry that achieves the smallest $\theta_{\max}$. At this point, the transmissivity threshold is $T_{\min} = 0.915$, and the maximum angle is $\theta_{\max} = 1.039$ rad $\approx 59°$.

D

SIMULATING A WHOLE LENS IN RCWA

After constructing the unit-cell library and assembling a complete phase profile, the next step is to simulate the full metalens and evaluate the accuracy of the design by determining its effective focal length. A direct application of RCWA, however, is complicated by the fact that the method is fundamentally periodic, whereas a metalens is a spatially varying, non-periodic structure. To overcome this, the lens is embedded into a carefully constructed one-dimensional RCWA supercell, allowing the entire device to be simulated within a formally periodic framework.
The metalens is represented as a one-dimensional supercell containing all individual unit-cells arranged according to their designed center positions and duty cycles. In order to bypass the periodicity of the simulation, padding is added around the lens, the unit-cell and the padding layer are shown in figure D.1. These padding regions are several times wider than the actual patterned area (typically three times the lens diameter) and are filled with a homogeneous highly absorbing medium to suppress the passing of light. Therefore the optical stack is modeled as a sequence of uniform and patterned layers:

1. an incident medium (air),
2. the patterned silicon nitride layer containing the lens profile ($n \approx 2$) shown in figure D.1 on the left,
3. an absorbing padding layer to block the light around the lens shown in figureD.1 on the right,
4. an output region (air) through which the transmitted field propagates.

The influence of the padding size was systematically investigated, showing that for padding factors of three times the lens diameter or larger, the position of the focal point remained constant. This behavior indicates that from this size and larger, the simulated lens can be considered effectively isolated from the artificial periodicity imposed by the RCWA method. This approach effectively isolates the lens from its periodic replicas, thereby mitigating the artificial periodicity inherent to RCWA simulations.

Figure D.2 shows a representative field-intensity map obtained with this approach, together with the corresponding on-axis intensity profile used to determine the focal point.

COMPUTATIONAL LIMIT OF USING RCWA FOR WHOLE LENS SIMULATION

In this research, the effectiveness of using RCWA for building unit-cell libraries has been re-evaluated and confirmed, as this approach has already been demonstrated successfully in several works [9], [24], [27]. The novel contribution here lies in the use of RCWA *supercells* to simulate entire metalenses and the interaction of the incident light with them. This method proved effective for small lenses; however, as the lens diameter increases, the computational cost grows rapidly. The parameter N_x, which represents the number of discrete grid points resolved along the design direction (i.e., the direction in which the metalens extends), becomes larger for lenses containing more unit-cells. Larger lenses include more distinct unit-cells across their radius, and to accurately resolve all of them, a finer spatial sampling is required. Since the RCWA computation scales with N_x, both memory usage and computation time increase significantly for larger lenses, making simulations of wide-aperture devices computationally expensive. The number of grid points in the patterned

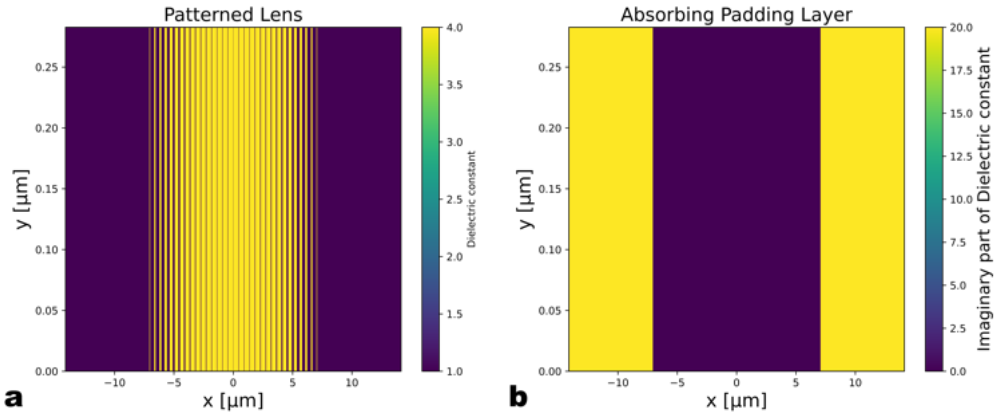

Figure D.1: Visualization of the Supercell Dielectric Layout and Absorbing Padding. **(a)** In-plane dielectric map of the patterned lens layer, showing alternating high-index Silicon Nitride bars and low-index slits arranged according to the designed phase profile for an example focal length of $f = 50\mu$m and padding of twice the size of the lens itself; **(b)** Imaginary part of the permittivity in the surrounding absorbing layer used to suppress artificial reflections and minimize the effect of the periodic boundary conditions. The padding and absorbing regions ensure that the simulated supercell effectively represents a single isolated lens.

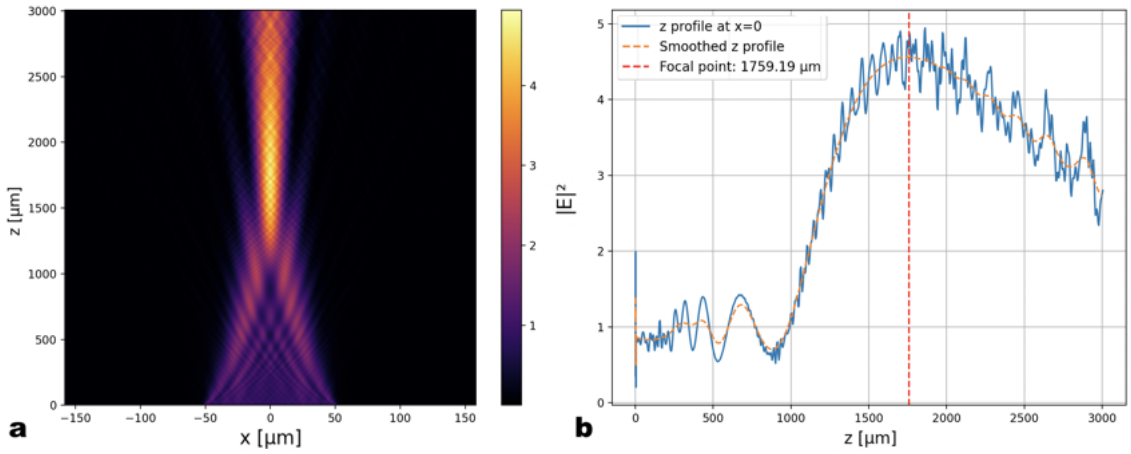

Figure D.2: Simulated Electric Field Intensity and Focal Point Determination. **(a)** The simulated electric field intensity $|E|^2$ in the $x-z$ plane, illustrating the focusing behavior of the full metalens; **(b)** The field intensity along the $x = 0$ line, which is used to determine the focal point. The red dashed line indicates the extracted focal point for a target focal length of $f = 2000\mu$m.

layer, N_x, is derived from the smallest feature that appears in the "supercell". First, the code determines the smallest lateral feature in the lens, i.e. either a slit (hole) width or the gap between two neighboring slits. To resolve this feature properly on the spatial grid, the in-plane grid step Δx is chosen as a fraction of it; in the code $\Delta x = \frac{f_{\min}}{3}$ so that at least three grid points span the smallest feature. The number of grid points in x is obtained by dividing the total supercell width by the desired grid step:

$$N_x = \left\lfloor \frac{a}{\Delta x} \right\rfloor,$$

where a is the total size of the supercell. As a result, N_x increases whenever the lens becomes wider. For smaller lenses, typically below 1000 μm in diameter, the simulations run smoothly, whereas for larger lenses the computation time and memory usage grow significantly, making the simulations increasingly lengthy.